remote sensing

MDPI

Article

Quantitative Inversion of Martian Hydrous Minerals Based on LSTM-1DCNN Model

Xinbao Liu [1,2,3], Ming Jin [1,2,*], Xiangnan Liu [3], Zhiming Yang [1,2], Zengqian Hou [1,2] and Xiaozhong Ding [1,2]

[1] Institute of Geology, Chinese Academy of Geological Sciences, Beijing 100037, China; liuxinbao@email.cugb.edu.cn (X.L.); zhiming.yang@cags.ac.cn (Z.Y.); houzengqian@126.com (Z.H.); xiaozhongding@sina.com (X.D.)
[2] National Geological Mapping Research Center of China Geological Survey, Beijing 100037, China
[3] School of Information Engineering, China University of Geosciences Beijing, Beijing 100083, China; liuxn@cugb.edu.cn
* Correspondence: jinmingjsh@163.com; Tel.: +86-134-0119-0327

Abstract: Hydrous minerals are significant indicators of the ancient aqueous environment on Mars, and orbital hyperspectral data are one of the most effective tools for obtaining information about the distribution of hydrous minerals on the Martian surface. However, prolonged weathering, erosion, and other external forces result in complex mixing effects, often weakening the spectral absorption features of individual minerals. This study proposes a quantitative inversion method for Martian hydrous minerals by integrating a radiative transfer model with a deep learning network. Based on the physics of the Hapke radiative transfer model, the single-scattering albedo spectra of mineral end members were obtained. Additionally, the Linear Spectral Mixture Model was employed to generate a large number of fully constrained mineral mixture samples, providing theoretical support for experimental data. An LSTM-1DCNN model was trained to establish a data-driven quantitative inversion framework. CRISM data were applied to the Eberswalde Crater region to retrieve the abundances of 21 hydrous minerals, including tremolite, opal, and serpentine. The average abundance of hydrous minerals was calculated to be 0.018, with a total area proportion of approximately 8%. Additionally, by analyzing the distribution areas of hydrous silicates, hydrous sulfates, and hydrous hydroxides, the water activity history of the region was inferred. The results align with findings from related studies and mineral spectral index results. By incorporating deep learning into traditional mixing models, this study identifies the distribution of various low-abundance hydrous minerals, enhancing the accuracy of Martian hydrous mineral inversion. It is expected to provide valuable references for the selection of landing sites for Tianwen-3 and support the smooth implementation of China's Mars exploration mission.

Keywords: spectral unmixing; quantitative inversion; Martian hydrous minerals; deep learning

check for updates

Academic Editors: Jan-Peter Muller, Long Xiao and Kaichang Di

Received: 25 November 2024
Revised: 24 December 2024
Accepted: 27 December 2024
Published: 30 December 2024

Citation: Liu, X.; Jin, M.; Liu, X.; Yang, Z.; Hou, Z.; Ding, X. Quantitative Inversion of Martian Hydrous Minerals Based on LSTM-1DCNN Model. *Remote Sens.* **2025**, *17*, 94. https://doi.org/10.3390/rs17010094

Copyright: © 2024 by the authors. Licensee MDPI, Basel, Switzerland. This article is an open access article distributed under the terms and conditions of the Creative Commons Attribution (CC BY) license (https://creativecommons.org/licenses/by/4.0/).

1. Introduction

The precise detection of mineral compositions on the Martian surface is crucial for revealing potential signs of life on Mars and constraining its evolutionary history. As one of the nearest terrestrial planets to Earth within the scope of human detection, previous studies have speculated that Mars may have hosted a habitable environment during the Noachian period based on the analysis of layered silicates [1,2]. The widespread hydrous minerals on the Martian surface reveal the history of the early aqueous environment. Although

a large number of qualitative studies have provided limited clues regarding early water activities on Mars [3–5], quantitative research of mineral assemblages and their relative abundances on the Martian surface can offer deeper constraints on the degree of aqueous alteration, formation conditions, and geological evolutionary history [6,7]. Therefore, the use of spectral data to estimate mineral abundances is of significant scientific value in advancing our understanding of the history of water.

Orbital hyperspectral data are the most effective means of rapidly obtaining information on mineral abundance information over large areas of Mars. Current methods for quantitative inversion of Mars using hyperspectral data include absorption-depth conversion [8,9] and spectral unmixing [10]. The absorption-depth conversion method estimates the relative content of the target mineral by approximating the intensity of the spectral absorption peaks. The absorption peak is influenced by factors, such as spectral mixing effects, leading to considerable uncertainty in this method. Therefore, it is primarily used for the qualitative analysis of Martian minerals.

In contrast, spectral unmixing is more commonly employed for quantitative inversion studies of Martian minerals. This method decomposes a mixed spectrum into multiple end-member spectra and obtains the proportional content of each end member. The dense mixing characteristics of Martian minerals result in the strong nonlinear characteristics of their mixing in visible-shortwave infrared reflectance [11] and the mixing of single-scattering albedo spectra, which is approximately a linear addition [12]. Therefore, spectral unmixing models generally require a combination of radiative transfer models for mineral inversion on Mars [13–15]. In Martian mineral abundance inversion, two methods of spectral unmixing have been developed based on different emphases: Multiple End-member Spectral Mixture Analysis (MESMA) [16] and sparse unmixing [17]. The MESMA method allows each pixel to use different end-member combinations during the unmixing process, thereby emphasizing the flexibility of end-member combinations. Combe et al. [18] applied a multiple-end-member linear spectral unmixing model to the Mars OMEGA dataset to identify the abundances of pyroxenes, olivines, gypsum, and other minerals in regions, such as Sytis Major, Aram Chaos, and the Arctic. Le Mouélic et al. [19] applied this method to analyze global Mars OMEGA data to retrieve the distribution and abundance of minerals, such as olivine, clinopyroxene, and orthopyroxene, on the Martian surface. However, because of the exponential increase in the number of models with an increase in the number of end members, this method is computationally intensive and unsuitable for situations with a large number of end members or complex ground object mixing. Therefore, it is challenging to achieve precise unmixing in regions with concentrated distributions of hydrous minerals, such as ancient Martian valleys and lakes with multi-mineral mixing.

Another method is the sparse unmixing algorithm, which focuses on optimizing the unmixing process through sparse constraints and emphasizes finding a combination of fewer end members to explain the mixed spectrum, which is suitable for specific sparsity assumptions. Sparse unmixing conditions can be created by applying sparse regularization methods, effectively reducing the computational cost of the least-squares algorithm in the unmixing process. Zhang et al. [20] used the Sparse Unmixing via Variable Splitting Augmented Lagrangian and TV (SUnSAL-TV) algorithm [21] to quantitatively invert the Mars Science Laboratory (MSL) landing zone, obtaining the abundances of seven minerals, including saponite, and the results were consistent with in situ analyses conducted by the MSL rover "Curiosity". Lin et al. [22] used the proposed Modified Sparse Unmixing (MSU) algorithm with Compact Reconnaissance Imaging Spectrometer for Mars (CRISM) data to quantitatively invert the abundance of three major hydrous minerals, including Fe/Mg phyllosilicates, prehnite, and kieserite, in the Gale Crater. Their results were consistent with the in situ detection results of "Curiosity". Lin [23] also proposed a new methodology

driven by a sparse unmixing model, performing the quantitative inversion of six CRISM images from three regions—Nili Fossae, Northeast of Syrtis Major, and Kashira Crater—and detected putative serpentine in the Nili Fossae region for the first time. In summary, existing sparse unmixing algorithms are limited by their computational complexity and thus restrict the number of end members. Moreover, Martian hydrous minerals have characteristics such as low content, scattered distribution, and uncertain background minerals [24], which can easily lead to the omission of end members and affect the inversion results. Therefore, sparse unmixing algorithms have limitations in the fine quantitative inversion of hydrous Martian minerals.

The quantitative inversion method based on deep learning is a type of data-driven method. It has been widely used in the field of ground object spectral unmixing with high accuracy [25–28]. At the same time, compared with the hybrid spectral decomposition methods widely used for Mars, the deep learning method reduces the cyclic iteration process and improves inversion efficiency. However, as it is challenging to obtain a large number of measured spectral label samples for the inversion of Martian minerals, the application of deep learning models to Martian mineral inversion is restricted. To address this issue, we used the Linear Spectral Mixing Model (LSMM) to rapidly generate large, labeled datasets using simulated abundance data and Earth sample spectral data.

This study proposes a quantitative inversion model based on the LSTM-1DCNN architecture, which integrates the advantages of MESMA and sparse unmixing, allowing for the flexible selection of end-member types and quantities while progressively applying sparsity through multiple thresholds. In addition, by intentionally expanding the variety of hydrous minerals included in the database, the model is particularly well-suited for the quantitative inversion of hydrous minerals on Mars.

2. Data

The data used in this study included end-member spectral and orbital hyperspectral data. The former was used to construct a Martian mineral end-member spectral library, generate labeled datasets, and train the LSTM-1DCNN model; the latter was used for the orbital data application of the quantitative inversion model.

2.1. End-Member Spectral Data

The rationality of the mineral end-member spectral library content had a significant influence on the training speed and prediction accuracy of the Martian mineral quantitative inversion model. This study relied on the USGS Spectral Library data (https://crustal.usgs.gov/speclab/QueryAll07a.php, accessed on 15 February 2024) and the Reflectance Experiment Laboratory (RELAB) data (https://speclib.rsl.wustl.edu/, accessed on 20 March 2024) to screen for proven Martian minerals and minerals of interest to construct a Martian mineral end-member spectral library. The USGS Spectral Library uses its Spectral Library Version 7 dataset, a spectral database compiled by the United States Geological Survey Spectral Analysis Laboratory and the Center for Geological, Geophysical, and Geochemical Sciences, to measure the reflectance spectra of minerals using laboratory, field, and aerial spectrometers. Diverse mineral species are suitable for use in spectral libraries. The RELAB spectral database, produced by Brown University and hosted by the PDS Geosciences Node, provides multiple types of spectral information for the same mineral, supporting research on spectral variation phenomena and addressing the practical issues of spectral diversity for the same object.

The MRO CRISM Type Spectra Library (https://crismtypespectra.rsl.wustl.edu/, accessed on 25 March 2024) was referenced to construct the end-member spectral library. This spectral library contains 31 typical minerals within 6 major categories: iron oxides

and primary silicates, ices, sulfates, phyllosilicates, carbonates, and other hydrated silicates and halides. These spectra were compiled into the Minerals Identified through the CRISM Analysis library, and similar laboratory spectra were obtained.

Thus, this study incorporated multiple spectral data of the same mineral into the Martian mineral spectral library to fully account for the effects of spectral variability. Additionally, synthetic positive and negative slope end members, as well as a zero-slope end member, were included in the spectral library to reflect the effects of dust or low-reflectance materials on the Martian surface and explain the spectral slope differences between the CRISM and laboratory spectra [29]. The end-member spectral library contained 199 spectral curves from 47 mineral types. The specific mineral end-member spectral library is listed in Table 1. Linear interpolation in MATLAB R2021b was used to resample all spectra so that the spectral library was aligned with the CRISM data in terms of spectral resolution.

Table 1. Mineral end-member spectral library.

Number	Name	Chemical Formula	Mineral Types	Spectrum Number
1	Alunite	$KAl_3(SO_4)_2(OH)_6$	Hydrated Sulfate	6
2	Bassanite	$CaSO_4 \cdot 0.5H_2O$	Hydrated Sulfate	1
3	Copiapite	$(Fe^{2+})_6(Fe^{3+})_2(SO_4)_4(OH)_2 \cdot 20H_2O$	Hydrous Sulfate	8
4	Gypsum	$CaSO_4 \cdot 2H_2O$	Hydrous Sulfate	2
5	Halotrichite	$FeAl_2(SO_4)_4 \cdot 22H_2O$	Hydrous Sulfate	2
6	Jarosite	$KFe_3(OH)_6(SO4)_2$	Hydrated Sulfate	5
7	Kieserite	$MgSO_4 \cdot H_2O$	Hydrated Sulfate	2
8	Letovicite	$(NH_4)HSO_4$	Ammonium Sulfate	2
9	Mascagnite	$(NH_4)_2SO_4$	Ammonium Sulfate	2
10	PolyHydratedMagnesiumSulfate	$MgSO_4 \cdot 7H_2O$	Hydrated Sulfate	1
11	Analcime	$NaAlSi_2O_6 \cdot H_2O$	Hydrated Silicate	1
12	Beidellite	$(Al,Fe^{3+})_2(Si,Al)_4O_{10}(OH)_2 \cdot nH_2O$	Hydrous Silicate	8
13	Chlorite	$(Mg,Fe^{2+})_5Al(Si_3Al)O_{10}(OH)_8$	Hydrous Silicate	5
14	Clinopyroxene	$(Ca,Na)(Mg,Fe,Al)(Si,Al)_2O_6$	Silicate	11
15	Epidote	$Ca_2Al_3(SiO_4)_3(OH)$	Hydrated Silicate	3
16	Halloysite	$Al_2Si_2O_5(OH)_4 \cdot nH_2O$	Hydrated Silicate	5
17	Illite	$K < 1\ (Al, R^{2+})_2\ [(Si,Al)\ Si_3O_{10}]\ [OH]_2\ \cdot nH_2O$	Hydrated Silicate	5
18	Kaolinite	$Al_2Si_2O_5(OH)_4$	Hydrated Silicate	6
19	Margarite	$KAl_3(AlSi_3O_{10})(OH)_2$	Silicate	1
20	Maskelynite	$NaAlSi_3O_8$	Silicate	2
21	Montmorillonite	$(Na,Ca)_{0.5}(Al,Mg)_2Si_4O_{10}(OH)_2 \cdot nH_2O$	Hydrated Silicate	6
22	Muscovite	$KAl_2(AlSi_3O_{10})(OH)_2$	Hydrated Silicate	5
23	Nontronite	$(Fe^{3+},Al)_2(Si,Al)_4O_{10}(OH)_2 \cdot nH_2O$	Hydrated Silicate	3
24	Olivine	$(Mg,Fe)_2SiO_4$	Silicate	10
25	Fayalite	$Mg < Fe\ (Mg,Fe)SiO_4$	Silicate	1
26	Forsterite	$Mg > Fe\ (Mg,Fe)SiO_4$	Silicate	1
27	Opal	$SiO_2 \cdot nH_2O$	Hydrated Silicate	5
28	Orthopyroxene	$(Mg,Fe)_2Si_2O_6$	Silicate	9
29	Plagioclase	$(Na,Ca)(Si,Al)_4O_8$	Silicate	9
30	Prehnite	$Ca_2Al(AlSi_3O_{10})(OH)_2$	Hydrous Silicate	1
31	Saponite	$(Na,Ca)_{0.5}(Mg,Fe)_3(Si_4O_{10})(OH)_2 \cdot nH_2O$	Hydrated Silicate	6
32	Serpentine	$Mg_3Si_2O_5(OH)_4$	Hydrous Silicates	4
33	Talc	$Mg_3Si_4O_{10}(OH)_2$	Hydrated Silicate	3
34	Tremolite	$Ca_2(Mg,Fe)_5Si_8O_{22}(OH)_2$	Hydrated Silicate	2
35	Vermiculite	$(Mg,Fe,Al)_3(Al,Si)_4O_{10}(OH)_2 \cdot 4H_2O$	Hydrated Silicate	4
36	Calcite	$CaCO_3$	Evaporite	9
37	Chloride	$(NH_4)Cl$	Evaporite	1
38	Magnesite	$MgCO_3$	Evaporite	13
39	MagnesiumSulphate	$MgSO_4$	Evaporite	1
40	Perchlorate	$R^{2+}(ClO_4)_2$	Evaporite	5
41	Siderite	$FeCO_3$	Evaporite	4
42	Diaspore	$AlO(OH)$	Aluminum Hydroxide	8
43	Goethite	$FeO(OH)$	Iron Hydroxide	5
44	Akaganeite	$FeO(OH,Cl)$	Iron Oxide	1
45	Hematite	Fe_2O_3	Iron Oxide	1
46	H_2OIce	H_2O	Oxide	1
47	dust		Unknown	3

R^{2+} represents a divalent metal cation.

2.2. Orbital Hyperspectral Data

In this study, the orbital hyperspectral image data (FRT000060dd) of the Eberswalde crater region on Mars were used to evaluate and apply the model. The Eberswalde crater underwent significant modifications in later stages, with its center located at 24°8′S, 33°39′W on Mars with a diameter of approximately 63 km. This crater region was once a potential landing site for the Mars Perseverance rover and holds great value for studying the early history of the Martian aqueous environment. As shown in Figure 1, the alluvial fan landform area is located within the crater. The hydromorphic landforms provide a strong indication of the hydrous mineral distribution, facilitating research on Martian hydrous minerals. The data were acquired using the Compact Reconnaissance Imaging Spectrometer for Mars (CRISM) on the Mars Reconnaissance Orbiter (MRO) and provided by NASA's Planetary Data System (PDS) website (https://pds-geosciences.wustl.edu/, accessed on 21 February 2024). The CRISM spectrometer consists of two sensors: a visible and near-infrared sensor (VNIR, 0.36–1.06 μm) and an infrared sensor (IR, 1.00–3.94 μm), with a total of 544 channels in hyperspectral mode. It can observe the Martian surface in two spatial resolution modes: 18 m/pixel (FRT) and 36 m/pixel (HRL/HRS). After removing bad data channels and channels severely affected by emission spectra, this study retained 232 channels in the 18 m/pixel spatial resolution mode, specifically bands 3–235 in the FRT mode. Data preprocessing of CRISM included photometric, atmospheric, and geometric corrections. All steps were performed using the ENVI plug-in CRISM Analysis Toolkit (CAT) 7.4. The plug-in was downloaded from the PDS (https://pds-geosciences.wustl.edu/missions/mro/crism.htm, accessed on 14 March 2024).

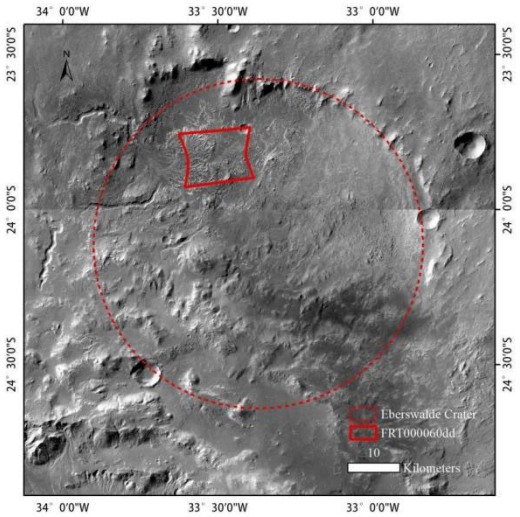


Figure 1. Overview map of the Eberswalde crater on Mars and the study area FRT000060dd. The Eberswalde crater underwent significant post-impact modifications, leaving only the northeastern crater rim intact. The FRT000060dd image is located northwest of the Eberswalde crater. The western part of the crater features a prominent valley where a river connects to the alluvial fan within the image coverage, forming a relatively complete aqueous landform. The base map data are CTX images.

3. Methods

The quantitative inversion model of Martian hydrous minerals constructed in this study involved three models: the radiative transfer model, the spectral mixing model, and the neural network model. Information flow was achieved between the models by assigning data features. The technical route used in this study is shown in Figure 2. This study's technical route mainly consisted of three parts. First, data preprocessing was performed, and the Hapke radiative transfer model was applied to enhance the spectral

features. Second, a spectral mixing model was used to construct a label dataset. Finally, a quantitative inversion model of Martian hydrous minerals was constructed based on the LSTM-1DCNN model, and CRISM images were used for the inversion of Martian hydrous minerals. The LSTM-1DCNN model is the core of the inversion model, which is composed of two sequential sub-networks: Long Short-Term Memory (LSTM) and a 1D Convolutional Neural Network (1DCNN). This design transforms the complex spectral unmixing problem into two simpler tasks: feature recognition and multivariate regression. By doing so, it reduces the overall complexity of the network structure while significantly enhancing the model's inversion speed. Each sub-network is only required to perform its respective task—qualitative identification or abundance inversion—based on the provided information. Consequently, the network depth does not need to be excessively deep, which further simplifies the structure. More importantly, this model allows the 1DCNN network to operate on the basis of qualitative identification, thereby reducing the impact of result non-uniqueness on inversion accuracy and effectively improving the inversion results.

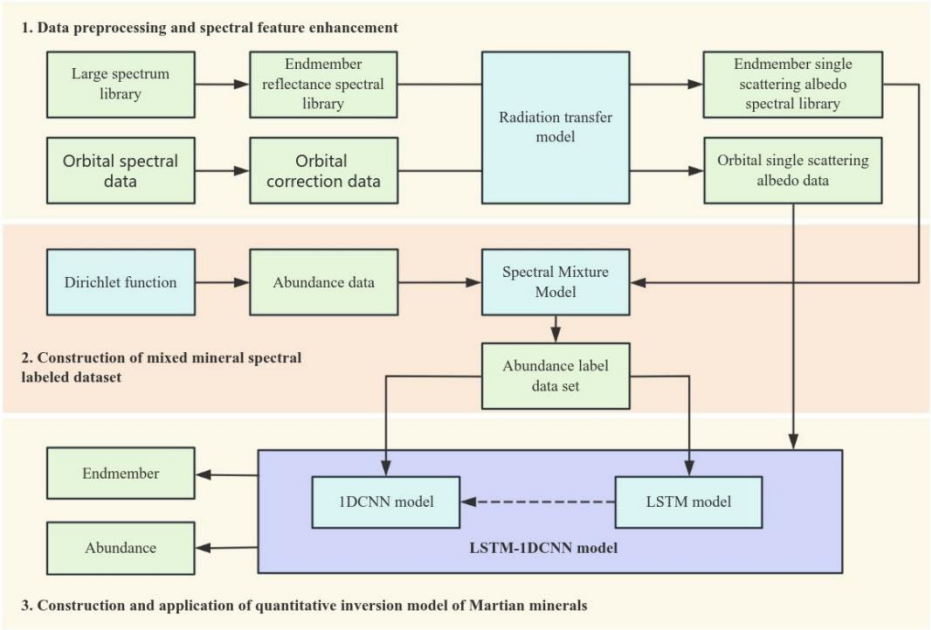


Figure 2. Technology roadmap.

3.1. Radiative Transfer Model

The quantitative inversion model in this study is essentially a data-driven model, so the accuracy of the simulated data is critical to the model's inversion performance. The mixing of various minerals on the Martian surface is a dense mixture that manifests as a highly nonlinear mixing pattern in the reflectance spectra. The direct application of linear spectral mixing methods results in a low accuracy. Therefore, this study introduced the Hapke radiative transfer model to convert reflectance into a single-scattering albedo, which represents the ratio of the part of the incident light scattered by the particle to the sum of the absorbed part and the scattered part of the particle [30]. This approach effectively reduced the spectral differences between the samples in the simulated dataset and the real samples, thereby improving inversion accuracy.

Bruce Hapke, the father of American planetary science, laid the foundation for a radiative transfer model of planetary surfaces. He established the Hapke radiative transfer model that connected macroscopic and microscopic properties to describe the scattering of sunlight on granular media, particularly on planetary regolith surfaces, and for the first time, derived the relationship between the reflectivity of mixed minerals and the optical and physical parameters of the medium when the particle size in a semi-infinite medium

was larger than the wavelength [30]. The function describing the relationship between reflectivity and single-scattering albedo is shown in Equation (1):

$$r = \frac{\omega\mu_0}{4(\mu_0+\mu)} \cdot [(1+B(g))P(g) + H(\mu_0,\omega)H(\mu,\omega) - 1] \quad (1)$$

where $\mu_0 = \cos(i)$, $\mu = \cos(e)$, i and e are the radiation incident angle and emission angle, respectively, g represents the phase angle, and ω is the single-scattering albedo, which is also the target of the radiative transfer model conversion. r represents the reflectance, which, in CRISM data, corresponds to the reflectance corrected for atmospheric and photometric effects. $B(g)$ is the backscatter function related to the phase angle g, describing the opposition effect. When the phase angle g is greater than 15°, the opposition effect can be ignored and the value of $B(g)$ begins to approach zero [11,22,31]. In this study, the phase angle of CRISM data FRT000060dd is greater than 42°, which is significantly beyond the 15° threshold identified in previous studies, so we set $B(g) = 0$. $P(g)$ is the phase function of the medium, which describes the probability of incident light being reflected in a certain direction. Assuming isotropic single scattering of particles, the phase function was set as $P(g) = 1$ [12]. $H(\mu,\omega)$ represents the multiple-scattering function. An approximation of $H(\mu,\omega)$ was proposed by Hapke, with an error within 4% compared to the true value [30], as shown in Equation (2):

$$H(\mu,\omega) = \frac{1+2\mu}{1+2\mu\sqrt{1-\omega}} \quad (2)$$

By substituting the above assumptions and Equation (2) into Equation (1), a simplified version of the Hapke radiative transfer model is derived, as shown in Equations (3) and (4). This simplified approach has been applied in Martian mineral inversion studies and its feasibility has been validated [22]. Considering that the phase angles and other parameters of the mineral end-member spectral library data and the FRT000060dd data from the study area meet the conditions for simplification, this study also adopts the simplified version of this model.

$$\sqrt{1-\omega} = \frac{\left[(\mu_0+\mu)^2\varphi^2 + (1+4\mu_0\mu\varphi)(1-\varphi)\right]^{1/2} - (\mu_0+\mu)\varphi}{1+4\mu_0\mu\varphi} \quad (3)$$

$$\varphi = 4\frac{\mu_0+\mu}{\mu_0}\frac{1}{(1+2\mu_0)(1+2\mu)}r \quad (4)$$

Based on Equations (3) and (4), the nonlinear solver function fsolve in MATLAB R2021b is used to calculate the single-scattering albedo data by inputting the reflectance data, the incidence, and the emission angle data.

3.2. Spectral Mixture Model

The single-scattering albedo spectrum of minerals exhibits an approximately linear additive relationship during the process of mineral mixing [30]. Therefore, a Linear Mixing Model (LMM) [9] was introduced to simulate spectral mixing, as shown in Equation (5). The study by Lin has already proven the feasibility of this simulated sample approach, with their results showing that the abundance error between simulated samples and real samples does not exceed 3% [23]. Although the accuracy of models trained on these data can only match the precision of the simulated data, it still meets the accuracy requirements for model predictions.

$$\omega_{\text{mix}} = \sum_{j=1}^{J} a_j\omega_j + k \quad (5)$$

where ω_{mix} represents the single-scattering albedo of the mixed minerals, ω_j is the single-scattering albedo of end-member j generated in Section 3.1, a_j is the end-member volume abundance produced by the Dirichlet distribution and satisfies the full constraints of $a_j > 0$

and $\sum a_j = 1$, and k is the generated random noise vector. Assuming that Martian surface minerals are uniformly mixed, the volume abundance is approximately equal to the relative geometric cross-section.

The role of the spectral mixing model is to simulate the single-scattering albedo of mixed minerals using the weighted average of the single-scattering albedo of the end members, thereby generating a large amount of label sample data. Based on the mineral complexity assumptions of the Martian surface, the number of effective end members within a pixel ranges from 5 to 8 [23]. The value of J was set to five mixing modes: 4, 5, 6, 7, and 8, representing the number of end members involved in the mixing. For each J value, 20,000 spectral label samples were randomly generated, resulting in a total of 100,000 spectral sample datasets. The dataset was randomly divided into training and test sets in a 4:1 ratio to train the model described in Section 3.3.

3.3. LSTM-1DCNN Model

3.3.1. LSTM Network

The task of mixed spectral end-member identification is similar to the multi-label classification problem in deep learning. Specific label features were extracted from the data, and binary existence labels were assigned to each label based on the confidence thresholds. This study specifically designed a qualitative network structure for the characteristics of Martian CRISM data. In this study, the LSTM network consists of a bidirectional long short-term memory (Bi-LSTM) layer, a dropout layer, a fully connected layer, and a sigmoid output layer. The input data for training the network consist of simulated mixed mineral spectral samples generated in Section 3.2, and the output is the existing confidence levels of 199 end members corresponding to the spectral library. The overall network structure is shown in Figure 3.

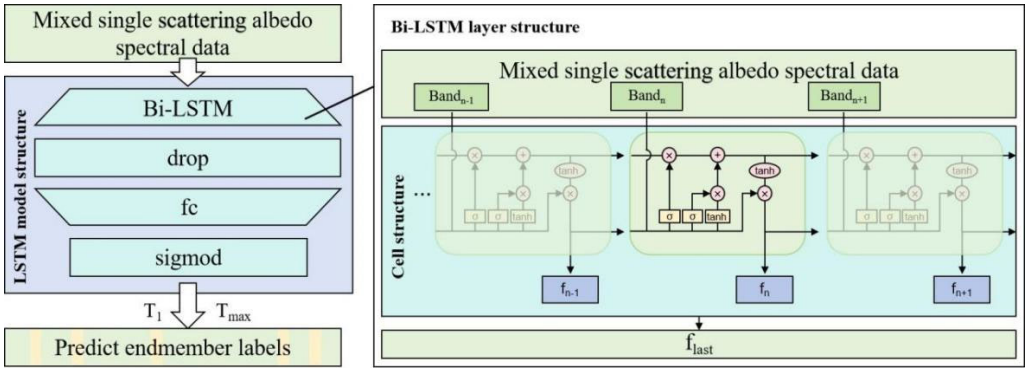


Figure 3. LSTM model structure diagram and Bi-LSTM layer structure diagram, where the LSTM layer neuron structure is referenced from Li et al. [32].

The Bi-LSTM layer is the feature extraction layer of the LSTM network. This layer has notable advantages in extracting one-dimensional data features through a unique gating mechanism, particularly when the data exhibit interdependence, which aligns well with the characteristics of hyperspectral data. The layered structure is illustrated in Figure 3. The cell uses the Forget Gate to select and discard cell state information. The sigm and tanh functions in the Input Gate determine which new information is stored in the cell state, allowing information to flow throughout the chain. Finally, the feature vector (f_n) is processed by sigm in the Output Gate, while tanh further updates the cell state. Each cell outputs features based on the previous cell state and input information [32], so that the final feature output (f_{last}) retains the information from the entire spectrum. The drop layer enhances the overall nonlinear prediction capability and generalization of the LSTM network. The fully connected layer aligns the number of features with the number of

end members, and the sigmoid layer converts the output into end-member confidence levels, facilitating the subsequent sparsification of end members based on a threshold. In this study, the LSTM network's outputs were binarized by setting a threshold T_1 for end-member confidence and the 199 output labels were divided into 0 and 1, where 0 represents an absence of an end member and 1 represents its presence. The T_1 threshold value was between 0 and 1 and primarily functioned to screen for potentially present end members. The specific value of T_1 should be determined based on the conditions of the study area and the CRISM data quality. The T_1 value is discussed in detail in Section 4.1 of this paper. Additionally, to ensure the number of identified end-member spectra did not exceed the input limit of the 1DCNN model, the total number of end members predicted as "1" was constrained by the T_{max} threshold, an integer greater than "0". This threshold ensures rational data transfer between the two subnetworks.

3.3.2. 1DCNN

This study addressed the problem of the process from end members to abundances by constructing a 1DCNN. To reduce model complexity and effectively extract features, the input section of the model was designed to consist of two concatenated parts, as shown in Figure 4. The first part of the input was the end-member spectral data output from the LSTM network in described Section 3.3.1, which was concatenated sequentially from left to right. If there were empty end-member spectral positions, they were filled with zeros, ensuring that the predicted end members were unified to the same size. The second part consisted of the corresponding mixed spectral data. In summary, the input format of the model was 232 × 11. The output of the model consists of abundance values for 10 corresponding spectra, satisfying the constraints of being greater than zero and summing to one. A network structure diagram of the 1DCNN, along with the input and output data flow, is shown in Figure 4.

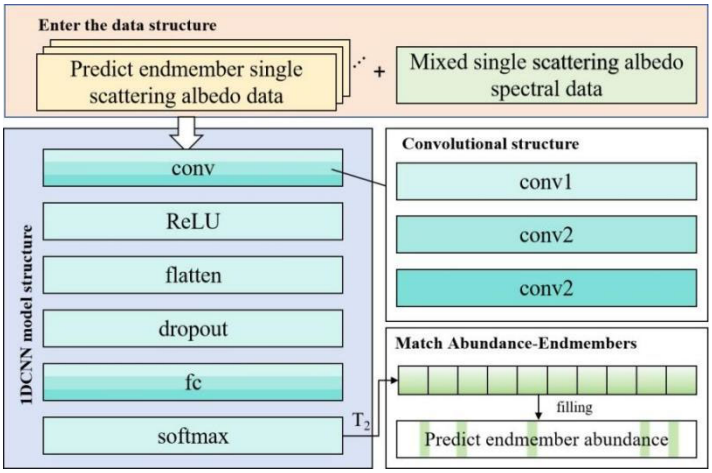


Figure 4. 1DCNN structure and data chart.

The 1DCNN was composed of three convolutional layers, the ReLU activation function layer, the flatten layer, three fully connected layers, and a softmax output layer. The three convolutional layers were used to progressively extract the features between the mixed spectra and the individual end-member spectra. The ReLU layer enhanced the nonlinear problem-solving capability of the model, and the weight relationship between the mixed mineral and end-member spectra was obtained by flatten layer and fully connected layers. The output of the 1DCNN achieved T_{max} fully constrained values through softmax. The prediction results were denoised by setting an abundance threshold of T_2 and retaining only end members with abundance values greater than T_2. This process effectively reduced

the impact of image noise on the experimental results and ensured the accuracy of the inversion outcomes. T_2 is a real number between 0 and 1 that serves to remove noise from the model's results. If T_2 is set too high, a large amount of valuable information may be lost; if set too low, the noise influence will be significant. Therefore, determining the value of T_2 requires expert judgment based on experimental results.

4. Results

4.1. LSTM Network Qualitative Training Result

The accurate identification of mineral end members is the basis for achieving refined abundance inversion. This study used an LSTM network implemented on the Kaggle platform (https://www.kaggle.com/, accessed on 20 September 2024) within the PyTorch 2.4.0 framework, leveraging a Tesla P100-PCIE-16GB GPU, a 4-core CPU, and 29GB of RAM. The LSTM network was trained using the binary cross-entropy loss function (BCELoss) and the Adam optimizer with a learning rate of 0.0005. The training dataset consisted of 80,000 samples, with 500 training epochs and a batch size of 64. The dataset used for training was generated using the Mineral End-member Spectral Library based on the Hapke radiative transfer model and the linear mixing model, resulting in a labeled dataset of 100,000 samples simulated in MATLAB 2021b. Each labeled sample consists of two parts: simulated spectra and end-member labels. The dataset was split into a training set and a test set in a 4:1 ratio. The input data comprise simulated mixed spectral data (80,000 $\times$ 232), where 80,000 represents the number of samples and 232 is the number of spectral bands. The data were simulated in MATLAB using the linear spectral mixing model. The output corresponds to the end-member label data (199 $\times$ 1), where 199 is the total number of end-member spectra. The output values are binary (0 or 1), indicating the presence or absence of the corresponding end-member. The output produced a variable number of labels based on the constraints of T_1 and $T_{\max}$. $T_{\max}$ was set to 10 according to the input structure of the 1DCNN. A comprehensive analysis of the LSTM network's output was conducted with respect to the T_1 value. The results for the LSTM network's accuracy, precision, recall, and F1 score on the test set as T_1 varies are shown in Figure 5: when T_1 = 0.25, the accuracy reaches its peak. Considering the class imbalance in the data, the F1 score is the primary metric of interest, peaking near T_1 = 0.2. Below this threshold, the recall continues to increase, indicating that some end members are still being missed. However, the precision drops sharply when $T_1 < 0.15$, indicating a significant increase in misclassification. Considering that an excessively high T_1 value in the qualitative network could lead to missed end-member extractions and a value too low could result in severe striping effects in the predicted results, this study determined that T_1 should be restricted to a range of 0.1–0.2 based on the combined performance of the four metrics mentioned above.

The LSTM network's output labels have a many-to-one relationship with mineral types. Identifications corresponding to different spectra of the same mineral should be considered successful. Therefore, we further merged the label results based on mineral types. This further reduces the possibility of non-uniqueness in the results and minimizes the errors caused by non-uniqueness. When T_1 = 0.1 and $T_{\max}$ = 10, the results of the 20,000-sample test set are shown in Figure 6. The average recognition accuracy of the 47 mineral types in the LSTM network is 97.76%, with more than half of the minerals' identification accuracy above 95%. Among them, the identification accuracy of plagioclase, calcite, and magnesite is relatively low, which were all below 93%. Therefore, the qualitative results of these minerals should be manually verified for their authenticity during application.

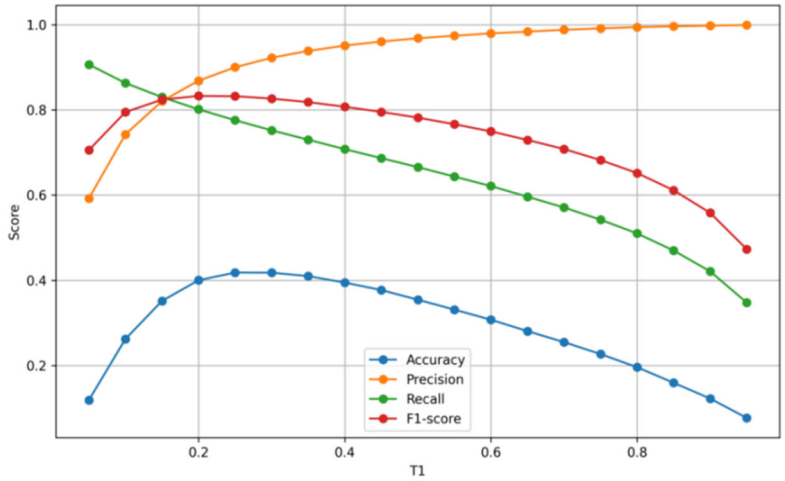


Figure 5. Model accuracy, precision, recall, and F1 score trends as T_1 changes.

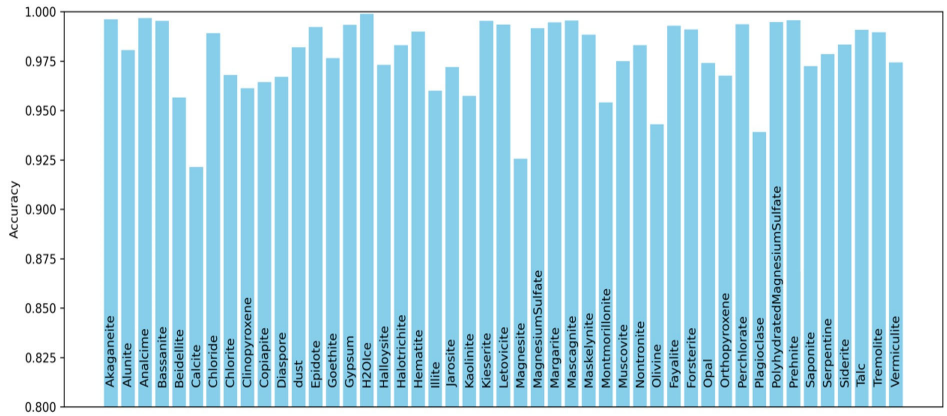


Figure 6. Qualitative network mineral identification accuracy chart.

4.2. 1DCNN Quantitative Training Results

The 1DCNN used was also implemented on the Kaggle platform using the PyTorch 2.4.0 framework with a Tesla P100-PCIE-16GB GPU, a 4-core CPU, and 29GB of RAM. The mean squared error (MSELoss) function and an Adam optimizer with a learning rate of 0.0005 were used to train the 1DCNN. The training dataset contained 80,000 samples, with a batch size of 64. The dataset used for training is similar to that used for the LSTM network, with the key difference being that the labeled samples consist of three parts: simulated mixed spectra, end-member spectral combinations, and abundance labels. The input data are a combination of mixed spectral data and end-member spectral data, with dimensions of 80,000 $\times$ 232 $\times$ 11, where 80,000 represents the number of samples, 232 is the number of spectral bands, and 11 corresponds to the mixed spectra and 10 individual end-member spectra. The output data consist of abundance labels for the 10 end members. The stability of the model's quantitative output is crucial for the inversion results. Training started with 100 batches and incrementally increased by 50 batches per round, continuing for six rounds. The correlation between predicted abundances on the test set and the true abundance labels for different training batches is shown in Figure 7, where a, b, c, d, e, and f represent the results for 1DCNN training batches of 100, 150, 200, 250, 300, and 350, respectively. The experimental results show that the average mean squared error (MSE) value on the test set was 0.0039 with smaller fluctuation, indicating the stability of the network's training results. The predicted results on the test set exhibited a significant positive correlation with the labels: the slope is k = 1 $\pm$ 0.04 and the intercept is b = 1 $\pm$ 0.012. Additionally, the scatter plot showed that as the label abundance value increased, the model's predictions

became more accurate, whereas lower abundance values resulted in greater prediction errors. This suggests that the randomness of the inversion results increased when the mineral abundance value was low, leading to noticeable noise in the image. Therefore, the T_2 threshold should be applied to remove the lower abundance results to reduce errors.

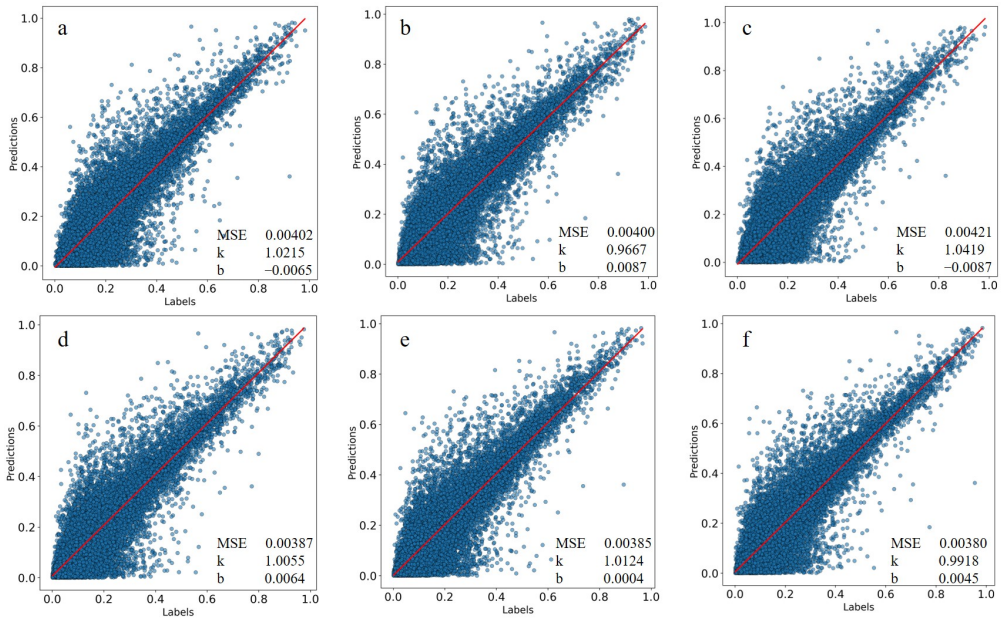


Figure 7. Scatter plot of the test set for multi-batch training of the quantitative network. Panels (**a**–**f**) represent the results for 1DCNN training batches of 100, 150, 200, 250, 300, and 350, respectively.

4.3. Application of LSTM-1DCNN Network Model in Track Data

The LSTM-1DCNN model was applied to the CRISM data for regional-scale mineral quantitative inversion to obtain an abundance of 35 minerals, with the statistical results shown in Figure 8, indicating that the inversion yielded abundance data for 35 minerals in the region. Excluding unknown mineral components, such as dust, the abundances of olivine, plagioclase, clinopyroxene, and maskelynite were generally high, with median abundance values of approximately 0.22, 0.24, 0.38, and 0.60, respectively. Other minerals generally had low abundances and were mostly concentrated below 0.2. The results indicated that the study area may contain a variety of low-abundance hydrous minerals and clay minerals. In addition, this study detected a small number of low-abundance H_2O ice signals. The abundance box plots reveal that the abundance of hydrous minerals of interest in this region is generally low, with an average abundance of 0.018. Before noise removal using the T_2 threshold, the median abundance of minerals like Kieserite was even as low as 0.01. A larger T_2 threshold has a significant impact on these important minerals. After comprehensive analysis, the T_2 threshold was set to 0.01 to retain information on hydrous minerals while removing noise. As shown in the figure, minerals such as letovicite and mascagnite exhibited high-abundance outliers, which were manually removed. This phenomenon may result from image noise, which significantly affects the spectra of the minerals.

Since a single pixel may contain multiple minerals, this study defined the total number of pixels occupied by all minerals as the total mineral distribution area. The ratio of the pixel count for each mineral to the total mineral distribution area was defined as the mineral area proportion. The inversion results, after removing mineral types significantly affected by noise such as mascagnite, letovicite, and copiaoite, were statistically analyzed, as shown in Figure 9. The figure illustrates the area proportion greater than 0.01% of 26 minerals within the study area. The statistical chart shows that the most widely distributed minerals in this

region are relatively ancient minerals, such as plagioclase, olivine, forsterite, clinopyroxene, and maskelynite, which is similar to the mineral distribution trend on the surface of Mars, which is generally dominated by ancient bedrock. Additionally, the statistical results also include 15 hydrous minerals with relatively low area proportions, such as epidote, tremolite, and opal, with a combined proportion of approximately 8%. Although the overall spatial distribution is relatively small, the hydrous mineral types are diverse and have various origins, providing diverse constraints for analyzing the evolutionary history of this region.

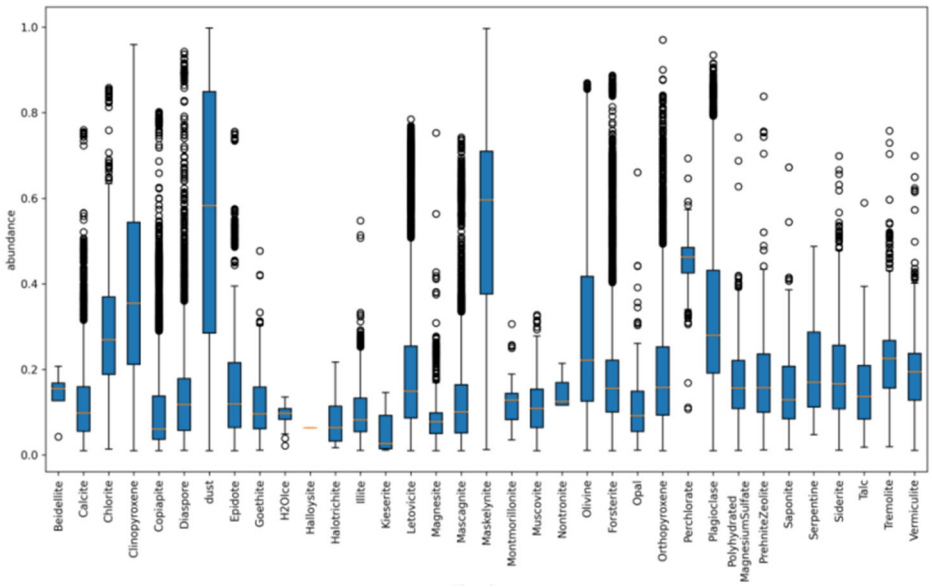


Figure 8. Box plot of predicted mineral abundance within the FRT000060dd map area.

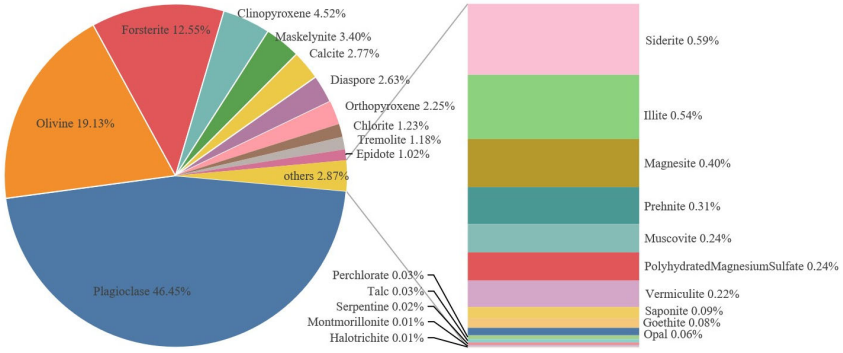


Figure 9. Statistical chart of the pixels occupied by major minerals.

Taking the inversion results of the highlights region in the northwest delta shown in Figure 10 as an example, the LSTM-1DCNN model developed in this study achieved accurate end-member and abundance predictions at the pixel scale. The pixel indicated by the red arrow in Figure 10a is located in the bright strip region of the delta. Its reflection characteristics in the image are significantly different from those of the background minerals. The inversion results of this study's model for this pixel identified 10 end members qualitatively, including 4 minerals: mascagnite, forsterite, orthopyroxene, and plagioclase, along with some low-reflectivity dust and unknown low-reflectivity materials. The identified end-member spectra overlap with the CRISM spectra at certain absorption peak positions. Additionally, a mixed spectrum was simulated using the end-member spectra and their corresponding abundances. It shows good consistency with the CRISM spectrum in both the absorption peak positions and overall absorption trends. The spectral angle

measurement between the two spectral curves was calculated as 0.004, and the inversion results of the LSTM-1DCNN model demonstrate a certain level of reliability.

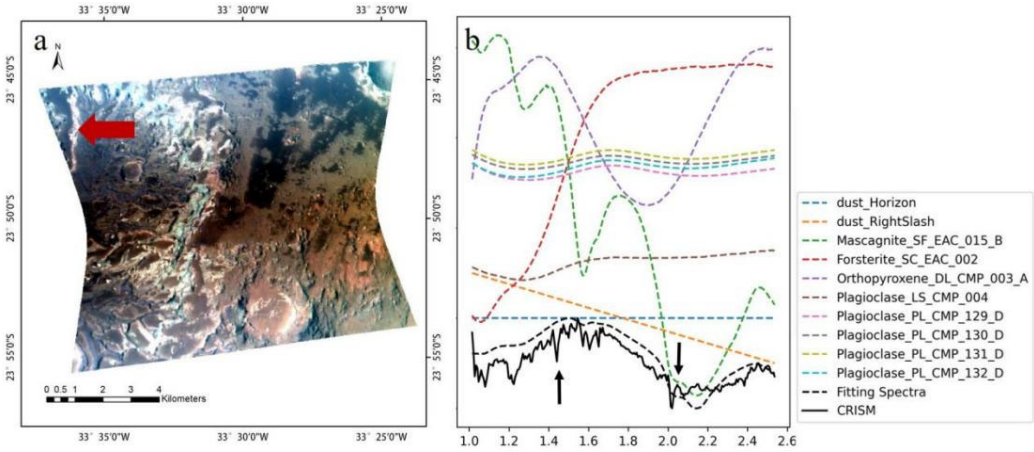


Figure 10. Comparison of model inversion results and CRISM data. (**a**) A false-color RGB image (red = 2.5295 μm, green = 1.5066 μm, blue = 1.0800 μm). The red arrow indicates the pixel location. In (**b**), the solid black line represents the orbital spectral curve of the pixel, whereas the dashed black line shows the simulated spectral curve based on the inversion results. The other dashed, colored lines correspond to the end-member spectra. The variations observed in the 1.4–1.55 μm range, marked by the arrow, result from instrumental errors [33], whereas the sharp peaks in the 1.9–2.1 μm range, also marked by an arrow, are due to atmospheric correction related to CO_2 [10].

The inversion results included 21 hydrous minerals, as shown in Figure 11. For clarity of analysis, the hydrous minerals were classified into three categories based on mineral type: hydrous sulfates, hydrous silicates, and hydrous hydroxides. The hydrous sulfate minerals, including halotrichite and kieserite, are primarily distributed in the high-brightness regions within the red rectangular areas (Figure 11a). Hydrous hydroxides, including diaspore and goethite, are mainly distributed in the low-elevation dark regions downstream of the delta (Figure 11b). Hydrous silicates are more diverse and include halloysite, illite, opal, and serpentine, which are primarily distributed in the bright regions of the figure, such as high-brightness outcrops at the edges of the delta and the rims of impact craters (Figure 11c).

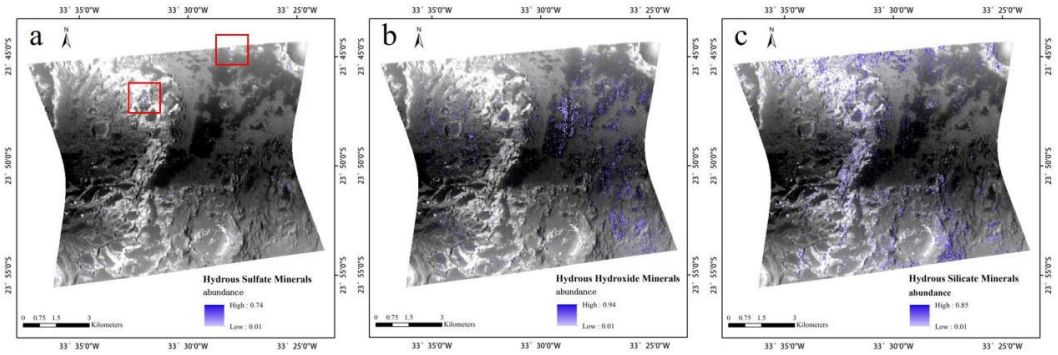


Figure 11. The distribution map of hydrous mineral types: (**a**) hydrous sulfate minerals, which have been highlighted with a red box, (**b**) hydrous hydroxide minerals, and (**c**) hydrous silicate minerals. The bottom figure is the gray-scale data for the 1.1652 μm.

5. Discussion

5.1. Mineral Type Identification

The qualitative study in this research uses an LSTM network combined with a T_1 threshold sparsity method to filter potential candidate end members from mixed spec-

tra. The experiments show that this identification method has advantages over existing Mars mineral identification methods in terms of identifying more end members and a faster recognition speed. Currently, Mars mineral identification studies mainly analyze spectral characteristics and use manually defined combinations of spectral characteristic parameters to determine mineral types [34,35]. However, spectral parameters typically only identify broad categories of minerals, and determining specific mineral subcategories often requires manual comparison, which is not only time-consuming but also highly subjective. In contrast, the LSTM qualitative network automatically extracts features through neural network layers and completes identification, improving speed while capturing more potential features. Additionally, Lin et al. [36] improved upon the Factor Analysis and Target Transformation [37] by proposing the Dynamic Aperture Factor Analysis and Target Transformation (DAFATT), which enables mineral type identification with spatial location information. However, only one end-member mineral can be identified at a time. The LSTM network achieved rapid identification of multiple minerals by leveraging end-member spectral libraries, significantly improving the efficiency of end-member recognition.

Previous studies have attempted to apply deep learning to Martian mineral spectral identification [38], demonstrating the feasibility of deep learning methods in Mars mineral identification. In this study, the LSTM network is considered part of the inversion process and needs to operate in coordination with the 1DCNN network. The output layer is configured for dynamic output, with fewer outputs than $T_{\max}$ and confidence greater than T_1, making the entire qualitative network more flexible. At the same time, some errors appeared in the qualitative identification results, with minerals exhibiting pronounced striping noise. Expert knowledge is required to assess these cases, posing a challenge to the accuracy of the LSTM network's identification.

5.2. Mineral Abundance Inversion

Extensive studies have been conducted on the mineral composition of the Martian surface. Kodikara et al. [39] proposed a method using deep neural networks to estimate the abundances of stilbite, montmorillonite, and epsomite from the reflectance spectra of ternary mineral mixtures. However, according to Hazen et al. [40], the confirmed number of Martian mineral species has reached 161, and many more Martian minerals remain undiscovered. In regions with hydrous mineral distribution, the mineral mixtures are more complex [24], and traditional binary and ternary mineral inversion methods are inadequate for the refined needs of Martian exploration. The quantitative inversion in this study is based on qualitative identification. The most widely used method for mineral abundance inversion on Mars is the least squares-based mathematical approach. This method iteratively identifies the mineral combinations and corresponding abundances that best match the measured spectra, thereby achieving abundance inversion. However, when there are five or more end members mixed within the model, least-squares regression often suffers from severe overfitting [41]. This overfitting leads to significant errors in the abundance inversion results. Moreover, least-squares regression involves extensive matrix computations, and the efficiency decreases exponentially with an increasing number of end members. Therefore, the number of end members in least-squares inversion is typically limited to 2–5. The goal of the quantitative model is similar to that of least-squares regression. This study addresses the problem by constructing a 1DCNN model, which simultaneously inputs the mixed spectra and the qualitative spectral results into the neural network. By utilizing multiple layers of neurons for nonlinear regression, the model identifies the weight relationships between the mixed spectra and the spectra of individual end members, thereby outputting the abundance values. This approach transforms the least-squares matrix-solving process into a deep learning-based nonlinear regression problem,

eliminating the iterative steps of least squares and significantly improving computational efficiency. The experimental results showed that using a ten-end-member mixture as an example, the 1DCNN model took 330.50 s to compute mineral abundances on the Kaggle platform with FRT000060dd data.

Additionally, the T_2 threshold was applied to the abundance inversion results to filter out end members with low contributions and poor stability during unmixing, thus enabling post-denoising of the model. Without setting a threshold, a wide distribution of low-abundance minerals may occur, making it difficult to ensure their authenticity. Considering the image quality of the FRT000060dd data in this study, the T_2 threshold was set to 0.01. If the image quality is lower, the T_2 value should be increased accordingly and further adjusted based on specific conditions.

5.3. Mineral Analysis of Typical Areas

The spectral index is an effective method for the rapid qualitative assessment of mineral distribution on the Martian surface. Generally, higher spectral index values indicate a higher abundance of the mineral. To ensure the accuracy of the experimental results, multiple inversion outcomes were integrated to derive more precise regional abundance data for specific minerals. The abundance of olivine and pyroxene obtained using the model in this study was compared with those obtained using the Olivine Index and the Pyronexe Index [42], as shown in Figure 12. The spatial distribution of minerals and their corresponding mineral indices in Figure 12 demonstrates a high degree of overlap, indicating that the mineral inversion results of this model are spatially reliable. Furthermore, panels (c) and (f) show a positive correlation between the model predictions abundance and the spectral index. This suggests that the abundance inversion results of this study are reliable in terms of abundance numerical trends. However, when the inversion abundance is low and the error is large, it is necessary to remove the low abundance mineral end element by the T_2 threshold, so as to improve the overall inversion accuracy and stability of the model. In Figure 12a, the two areas marked with red boxes have been identified by the model in this study as halloysite distribution zones. However, given that the absorption positions of halloysite and olivine overlap near 1 μm, and there is strong absorption around 1.36–1.45 μm, which is close to the band positions used in the Olivine Index, misidentification may have occurred. Therefore, the halloysite identified in this study has also been tentatively included to participate in the analysis of olivine abundance. The specific mineral type requires further investigation and discussion. Previously, Wu et al. [43] used collaborative sparse unmixing to quantitatively retrieve minerals in this region, obtaining six minerals, including pyroxene, which were validated using mineral spectra. The distributions of pyroxene, siderite, and plagioclase obtained in this study are consistent with their results, which validates the reliability of the inversion results in this research. Furthermore, this study identified 28 reliable mineral types in the same image, representing a significant improvement in the number of retrieved mineral end members. This demonstrates that the model is more suitable for mineral abundance inversion in scenarios with complex mineral mixing.

The typical delta landforms in this region indicate the presence of early liquid water activity [44]. In this study, the model's ability to accurately identify various mineral types was fully utilized, revealing a wide variety of hydrous minerals across the region. The inversion results show that the region exhibits overall characteristics of low hydrous mineral abundance, small area coverage, and high diversity of mineral types; moreover, their origins are mostly associated with water, consistent with the ancient environment implied by the deltaic water-related geomorphology. Furthermore, the presence of different types of hydrous minerals indicates diverse aqueous environments. High abundances of

pyroxene and other silicate rock-forming minerals, along with various hydrous silicate minerals, were found on the steep slopes of the bright regions along the delta edges, as shown in Figures 12 and 13. Based on the overall environmental context of the region, it is hypothesized that prolonged liquid water activity enabled silicates in the bedrock to either directly absorb water or chemically react with it to form hydrous minerals. Alternatively, hydrous minerals transported downstream by rivers may have been deposited in the alluvial fan, where steeper slopes facilitated the exposure of these ancient minerals. In contrast, dark regions with hydrous hydroxide minerals correspond to the low-elevation hillock in Figure 13, with little to no olivine or pyroxene present. This study suggests that the region once hosted a long-standing paleolake. Large quantities of cations in the lake water likely precipitated as hydroxides in an oxidizing environment, accumulating and covering the original silicate substrate—a process also observed in research on ancient marine environments on Earth [45]. The small crater in the northeast of the delta presented in Figure 1 shows no evidence of fluvial erosion, indicating that it formed after water activity ceased. However, its crater edges contain high abundances of hydrous minerals. These deep-seated minerals were likely excavated by the impact. Therefore, we hypothesize that more hydrous minerals may be buried under a layer of dust.

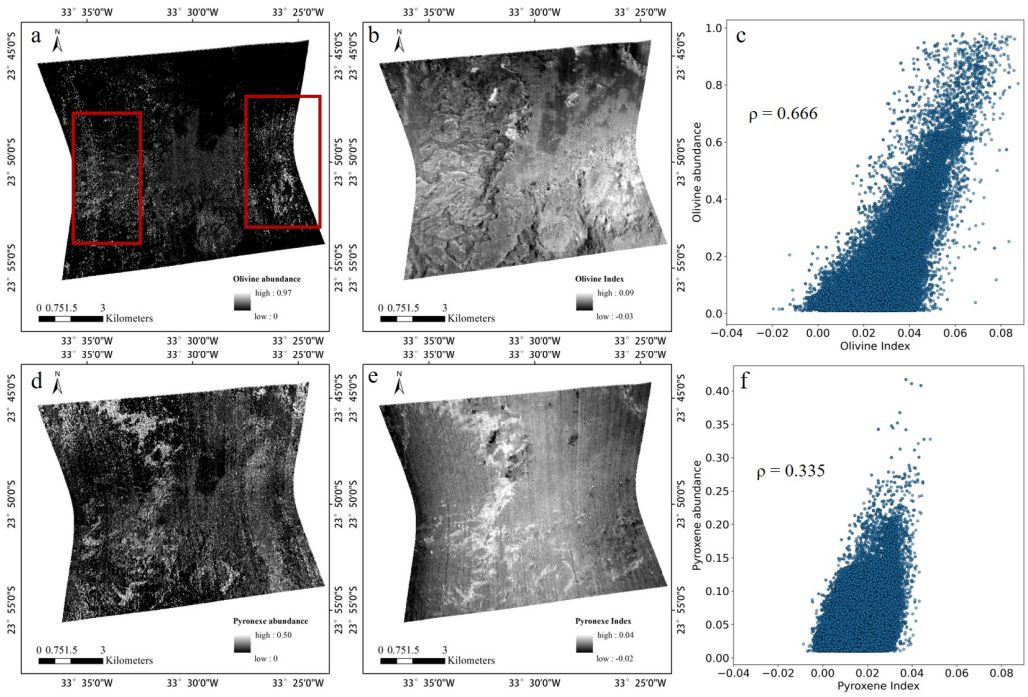


Figure 12. A comparison between mineral abundance inversion results and mineral spectral indices. Panels (**a**,**b**) represent the Olivine abundance and Olivine Index. The red rectangular region in Panel (**a**) represents a potential olivine distribution area. Panel (**c**) illustrates the scatter plot corresponding to the data presented in Panels (**a**,**b**); the Pearson Correlation Coefficient (ρ) between the two variables in Panel (**c**) is 0.666, indicating a moderately strong positive correlation. Panels (**d**,**e**) represent the Pyroxene abundance and Pyroxene Index. Panel (**f**) illustrates the scatter plot corresponding to the data presented in Panels (**d**,**e**); the ρ between the two variables in Panel (**f**) is 0.335, indicating a certain positive correlation.

The map area also displays a large number of low-abundance ammonium sulfate signals as shown in Figure 8. Previous, Manning et al. [46] hypothesized that ammonium sulfate minerals on Mars form when significant amounts of atmospheric nitrogen are fixed into soil nitrates and subsequently transported and enriched by groundwater in sulfur-rich environments. In this study, mascagnite and letovicite were included as end members in the mineral end-member spectral library because preliminary observations indicated that the

CRISM spectral absorption peaks in the study area overlapped with those of ammonium sulfate minerals. Sefton-Nash et al. [47] detected absorption signals of ammonium sulfate minerals, such as mascagnite and letovicite, in the Iani Chaos region. As Iani Chaos is near the Eberswalde Crater, similar environmental conditions were more likely to produce comparable mineral compositions, providing a reference for the mineral composition in the study area. However, the inversion results revealed that the spatial distribution trends closely aligned with the orbiter's movement direction, forming a distinct strip pattern inconsistent with the natural distribution of minerals. As a result, these minerals were manually removed by T_2 Threshold. This phenomenon may have resulted from image noise, which significantly affected the mineral spectra. Based on expert knowledge, these minerals were classified as unreliable, requiring further in-depth investigation in future studies.

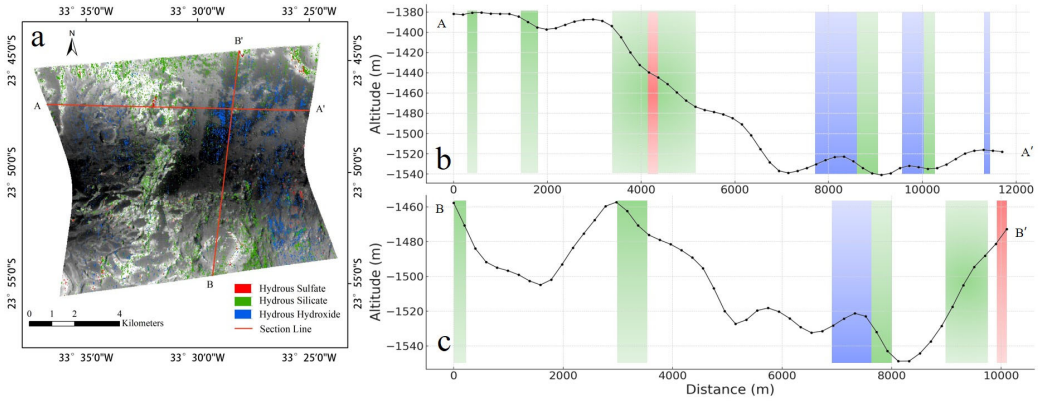


Figure 13. Horizontal and vertical elevation distribution maps of the three types of hydrous minerals. (**a**) The horizontal distribution of three types of hydrous minerals: hydrous sulfate minerals, hydrous hydroxide minerals, and hydrous silicate minerals. (**b**,**c**) The AA′ and BB′ cross-sectional profiles corresponding to (**a**), respectively, showing the elevation distribution of different minerals along and near the section lines.

6. Conclusions

This study presents a quantitative inversion model of Martian hydrous minerals based on the LSTM-1DCNN model for inversion Martian mineral abundances using CRISM hyperspectral data. The model comprises two subnetworks: the LSTM network, which is used for qualitative identification of end members in Martian mixed minerals, simplifies the overall model scale and enhances the accuracy of hydrous mineral inversion, while the 1DCNN performs quantitative determination of Martian mineral end members, effectively improving unmixing efficiency. The Hapke radiative transfer model is used to convert Martian mineral end-member spectra into single-scattering albedo spectra, and the Linear Spectral Mixing Method is employed to construct a labeled dataset for model training. The testing results show that this model achieves an average accuracy of 97.76% in qualitative recognition and an average MSE of 0.0039 in quantitative inversion. Using the LSTM-1DCNN model, the CRISM data enabled the inversion of the abundances of 31 high-confidence minerals in the Eberswalde crater area, including 21 hydrous minerals, with olivine and pyroxene abundance results showing high spatial correlation with mineral spectral indices. The model has high inversion accuracy and high potential to be applied to the entire Martian surface.

Author Contributions: Conceptualization, M.J. and X.L. (Xinbao Liu); methodology, M.J. and X.L. (Xinbao Liu); software, X.L. (Xinbao Liu); validation, X.L. (Xinbao Liu), M.J. and X.D.; formal analysis, X.L. (Xinbao Liu); investigation, X.L. (Xinbao Liu); resources, X.L. (Xinbao Liu); data curation, X.L. (Xinbao Liu); writing—original draft preparation, X.L. (Xinbao Liu); writing—review and editing,

X.L. (Xinbao Liu), M.J., X.L. (Xiangnan Liu), Z.Y., Z.H. and X.D.; visualization, X.L. (Xinbao Liu), M.J. and X.L. (Xiangnan Liu); supervision, M.J; project administration, M.J.; funding acquisition, M.J., Z.Y., Z.H. and X.D. All authors have read and agreed to the published version of the manuscript.

Funding: This research was funded by the National Natural Science Foundation of China (Grant No. 42302266), the Fundamental Research Funds of the Chinese Academy of Geological Sciences (Grant No. J2412), and the National Key Research and Development Program of China (2024YFF0807700).

Data Availability Statement: The original contributions presented in the study are included in the article, further inquiries can be directed to the corresponding author.

Conflicts of Interest: The authors declare no conflicts of interest.

References

1. Bishop, J.L.; Loizeau, D.; McKeown, N.K.; Saper, L.; Dyar, M.D.; Des Marais, D.J.; Parente, M.; Murchie, S.L. What the ancient phyllosilicates at Mawrth Vallis can tell us about possible habitability on early Mars. *Planet. Space Sci.* **2013**, *86*, 130–149. [CrossRef]
2. Bibring, J.-P.; Langevin, Y.; Mustard, J.F.; Poulet, F.O.; Arvidson, R.; Gendrin, A.; Gondet, B.; Mangold, N.; Pinet, P.; Forget, F.; et al. Global Mineralogical and Aqueous Mars History Derived from OMEGA/Mars Express Data. *Science* **2006**, *312*, 400–404. [CrossRef] [PubMed]
3. McKeown, N.K.; Bishop, J.L.; Noe Dobrea, E.Z.; Ehlmann, B.L.; Parente, M.; Mustard, J.F.; Murchie, S.L.; Swayze, G.A.; Bibring, J.P.; Silver, E.A. Characterization of phyllosilicates observed in the central Mawrth Vallis region, Mars, their potential formational processes, and implications for past climate. *J. Geophys. Res. Planets* **2009**, *114*, E00D10. [CrossRef]
4. Noe Dobrea, E.Z.; Bishop, J.L.; McKeown, N.K.; Fu, R.; Rossi, C.M.; Michalski, J.R.; Heinlein, C.; Hanus, V.; Poulet, F.; Mustard, R.J.F.; et al. Mineralogy and stratigraphy of phyllosilicate-bearing and dark mantling units in the greater Mawrth Vallis/west Arabia Terra area: Constraints on geological origin. *J. Geophys. Res. Planets* **2010**, *115*, E00D19. [CrossRef]
5. Ruesch, O.; Poulet, F.; Vincendon, M.; Bibring, J.P.; Carter, J.; Erkeling, G.; Gondet, B.; Hiesinger, H.; Ody, A.; Reiss, D. Compositional investigation of the proposed chloride-bearing materials on Mars using near-infrared orbital data from OMEGA/MEx. *J. Geophys. Res. Planets* **2012**, *117*, E00J13. [CrossRef]
6. Ehlmann, B.L.; Berger, G.; Mangold, N.; Michalski, J.R.; Catling, D.C.; Ruff, S.W.; Chassefière, E.; Niles, P.B.; Chevrier, V.; Poulet, F. Geochemical Consequences of Widespread Clay Mineral Formation in Mars' Ancient Crust. *Space Sci. Rev.* **2012**, *174*, 329–364. [CrossRef]
7. Poulet, F.; Carter, J.; Bishop, J.L.; Loizeau, D.; Murchie, S.M. Mineral abundances at the final four curiosity study sites and implications for their formation. *Icarus* **2014**, *231*, 65–76. [CrossRef]
8. Sunshine, J.M.; Pieters, C.M. Estimating Modal Abundances from the Spectra of Natural and Laboratory Pyroxene Mixtures Using the Modified Gaussian Model. *J. Geophys. Res. Planets* **1993**, *98*, 9075–9087. [CrossRef]
9. Poulet, F.; Mangold, N.; Loizeau, D.; Bibring, J.P.; Langevin, Y.; Michalski, J.; Gondet, B. Abundance of minerals in the phyllosilicate-rich units on Mars. *Astron. Astrophys.* **2008**, *487*, L41–L44. [CrossRef]
10. Keshava, N.; Mustard, J.F. Spectral unmixing. *IEEE Signal Process. Mag.* **2002**, *19*, 44–57. [CrossRef]
11. Mustard, J.F.; Pieters, C.M. Photometric phase functions of common geologic minerals and applications to quantitative analysis of mineral mixture reflectance spectra. *J. Geophys. Res. Solid Earth* **1989**, *94*, 13619–13634. [CrossRef]
12. Hapke, B. *Theory of Reflectance and Emittance Spectroscopy*; Cambridge University Press: Cambridge, UK, 2012.
13. Liu, Y.; Stachurski, F.; Liu, Z.; Zou, Y. Quantitative assessment of water content and mineral abundances at Gale crater on Mars with orbital observations. *Astron. Astrophys.* **2020**, *637*, A79. [CrossRef]
14. Liu, Y.; Glotch, T.D.; Scudder, N.A.; Kraner, M.L.; Condus, T.; Arvidson, R.E.; Guinness, E.A.; Wolff, M.J.; Smith, M.D. End-member identification and spectral mixture analysis of CRISM hyperspectral data: A case study on southwest Melas Chasma, Mars. *J. Geophys. Res. Planets* **2016**, *121*, 2004–2036. [CrossRef]
15. Liu, Y.; Goudge, T.A.; Catalano, J.G.; Wang, A. Spectral and stratigraphic mapping of hydrated minerals associated with interior layered deposits near the southern wall of Melas Chasma, Mars. *Icarus* **2018**, *302*, 62–79. [CrossRef]
16. Roberts, D.A.; Gardner, M.; Church, R.; Ustin, S.; Scheer, G.; Green, R.O. Mapping Chaparral in the Santa Monica Mountains Using Multiple Endmember Spectral Mixture Models. *Remote Sens. Environ.* **1998**, *65*, 267–279. [CrossRef]
17. Iordache, M.-D.; Bioucas-Dias, J.M.; Plaza, A. Sparse Unmixing of Hyperspectral Data. *IEEE Trans. Geosci. Remote Sens.* **2011**, *49*, 2014–2039. [CrossRef]
18. Combe, J.P.; Le Mouélic, S.; Sotin, C.; Gendrin, A.; Mustard, J.F.; Le Deit, L.; Launeau, P.; Bibring, J.P.; Gondet, B.; Langevin, Y.; et al. Analysis of OMEGA/Mars Express data hyperspectral data using a Multiple-Endmember Linear Spectral Unmixing Model (MELSUM): Methodology and first results. *Planet. Space Sci.* **2008**, *56*, 951–975. [CrossRef]

19. Mouélic, S.L.; Sarago, V.; Combe, J.-P.; Massé, M.; Bourgeois, O.; Mangold, N.; Bibring, J.-P.; Gondet, B.; Langevin, Y.; Sotin, C. Global Mapping of Minerals on Mars with OMEGA Hyperspectral Data: Results of a Linear Unmixing Approach. In Proceedings of the 40th Lunar and Planetary Science Conference, Woodlands, TX, USA, 23–27 March 2009.
20. Zhang, X.; Shuai, T.; Lin, H. Abundance retrieval of hydrous minerals around the mars science laboratory landing site. *Planet. Space Sci.* **2016**, *121*, 76–82.
21. Iordache, M.-D.; Bioucas-Dias, J.M.; Plaza, A. Total Variation Spatial Regularization for Sparse Hyperspectral Unmixing. *IEEE Trans. Geosci. Remote Sens.* **2012**, *50*, 4484–4502. [CrossRef]
22. Lin, H.; Zhang, X. Retrieving the hydrous minerals on Mars by sparse unmixing and the Hapke model using MRO/CRISM data. *Icarus* **2017**, *288*, 160–171. [CrossRef]
23. Lin, H.; Mustard, J.F.; Zhang, X. A methodology for quantitative analysis of hydrated minerals on Mars with large endmember library using CRISM near-infrared data. *Planet. Space Sci.* **2019**, *165*, 124–136. [CrossRef]
24. Carter, J.; Poulet, F.; Bibring, J.-P.; Mangold, N.; Murchie, S. Hydrous minerals on Mars as seen by the CRISM and OMEGA imaging spectrometers: Updated global view. *J. Geophys. Res. Planets* **2013**, *118*, 831–858. [CrossRef]
25. Chen, J.; Yang, C.; Zhang, L.; Yang, L.; Bian, L.; Luo, Z.; Wang, J. TCCU-Net: Transformer and CNN Collaborative Unmixing Network for Hyperspectral image. *IEEE J. Sel. Top. Appl. Earth Obs. Remote Sens.* **2024**, *17*, 8073–8089. [CrossRef]
26. Wang, B.; Yao, H.; Song, D.; Zhang, J.; Gao, H. SSF-Net: A Spatial–Spectral Features Integrated Autoencoder Network for Hyperspectral Unmixing. *IEEE J. Sel. Top. Appl. Earth Obs. Remote Sens.* **2023**, *17*, 1781–1794. [CrossRef]
27. Shao, Y.; Liu, Q.; Xiao, L. IVIU-Net: Implicit Variable Iterative Unrolling Network for Hyperspectral Sparse Unmixing. *IEEE J. Sel. Top. Appl. Earth Obs. Remote Sens.* **2023**, *16*, 1756–1770. [CrossRef]
28. Sun, L.; Chen, Y.; Li, B. SISLU-Net: Spatial Information-Assisted Spectral Information Learning Unmixing Network for Hyperspectral Images. *Remote Sens.* **2023**, *15*, 817. [CrossRef]
29. Poulet, F.; Mangold, N.; Platevoet, B.; Bardintzeff, J.M.; Sautter, V.; Mustard, J.F.; Bibring, J.P.; Pinet, P.; Langevin, Y.; Gondet, B.; et al. Quantitative compositional analysis of martian mafic regions using the MEx/OMEGA reflectance data. *Icarus* **2009**, *201*, 84–101. [CrossRef]
30. Hapke, B. Bidirectional reflectance spectroscopy: 1. Theory. *J. Geophys. Res. Solid Earth* **1981**, *86*, 3039–3054. [CrossRef]
31. Fraeman, A.A.; Arvidson, R.E.; Murchie, S.L.; Rivkin, A.; Bibring, J.P.; Choo, T.H.; Gondet, B.; Humm, D.; Kuzmin, R.O.; Manaud, N.; et al. Analysis of disk-resolved OMEGA and CRISM spectral observations of Phobos and Deimos. *J. Geophys. Res. Planets* **2012**, *117*, E00J15. [CrossRef]
32. Li, F.; Ren, G.; Lee, J. Multi-step wind speed prediction based on turbulence intensity and hybrid deep neural networks. *Energy Convers. Manag.* **2019**, *186*, 306–322. [CrossRef]
33. Langevin, Y.; Bibring, J.P.; Montmessin, F.; Forget, F.; Vincendon, M.; Douté, S.; Poulet, F.; Gondet, B. Observations of the south seasonal cap of Mars during recession in 2004–2006 by the OMEGA visible/near-infrared imaging spectrometer on board Mars Express. *J. Geophys. Res. Planets* **2007**, *112*, E08S12. [CrossRef]
34. Mustard, J.F.; Murchie, S.L.; Pelkey, S.M. Hydrated silicate minerals on Mars observed by the Mars Reconnaissance Orbiter CRISM instrument. *Nature* **2008**, *454*, 305–309. [CrossRef] [PubMed]
35. Ehlmann, B.L.; Mustard, J.F.; Swayze, G.A.; Clark, R.N.; Bishop, J.L.; Poulet, F.; Marais, D.J.D.; Roach, L.H.; Milliken, R.E.; Wray, J.J.; et al. Identification of hydrated silicate minerals on Mars using MRO-CRISM: Geologic context near Nili Fossae and implications for aqueous alteration. *J. Geophys. Res. Planets* **2009**, *114*, E00D08. [CrossRef]
36. Lin, H.; Tarnas, J.D.; Mustard, J.F.; Zhang, X.; Wei, Y.; Wan, W.; Klein, F.; Kellner, J.R. Dynamic aperture factor analysis/target transformation (DAFA/TT) for Mg-serpentine and Mg-carbonate mapping on Mars with CRISM near-infrared data. *Icarus* **2021**, *355*, 114168. [CrossRef]
37. Thomas, N.H.; Bandfield, J.L. Identification and refinement of martian surface mineralogy using factor analysis and target transformation of near-infrared spectroscopic data. *Icarus* **2017**, *291*, 124–135. [CrossRef]
38. Saranathan, A.M.; Parente, M. Adversarial feature learning for improved mineral mapping of CRISM data. *Icarus* **2021**, *355*, 114107. [CrossRef]
39. Kodikara, G.R.L.; McHenry, L.J.; van der Meer, F.D. Application of deep learning and spectral deconvolution for estimating mineral abundances of zeolite, Mg-sulfate and montmorillonite mixtures and its implications for Mars. *Planet. Space Sci.* **2022**, *223*, 105579. [CrossRef]
40. Hazen, R.M.; Downs, R.T.; Morrison, S.M.; Tutolo, B.M.; Blake, D.F.; Bristow, T.F.; Chipera, S.J.; McSween, H.Y.; Ming, D.; Morris, R.V.; et al. On the Diversity and Formation Modes of Martian Minerals. *J. Geophys. Res. Planets* **2023**, *128*, e2023JE007865. [CrossRef]
41. Jin, M.; Ding, X.; Han, H.; Pang, J.; Wang, Y. An improved method combining Fisher transformation and multiple endmember spectral mixture analysis for lunar mineral abundance quantification using spectral data. *Icarus* **2022**, *380*, 115008. [CrossRef]

42. Viviano, C.E.; Seelos, F.P.; Murchie, S.L.; Kahn, E.G.; Seelos, K.D.; Taylor, H.W.; Taylor, K.; Ehlmann, B.L.; Wiseman, S.M.; Mustard, J.F.; et al. Revised CRISM spectral parameters and summary products based on the currently detected mineral diversity on Mars. *J. Geophys. Res. Planets* **2014**, *119*, 1403–1431. [CrossRef]
43. Wu, X.; Zhang, X.; Lin, H. Retrieval of Mineral Abundances of the Delta Region in Eberswalde, Mars. *Int. Arch. Photogramm. Remote Sens. Spat. Inf. Sci.* **2017**, *42*, 171–176. [CrossRef]
44. Malin, M.C.; Edgett, K.S. Evidence for Persistent Flow and Aqueous Sedimentation on Early Mars. *Science* **2003**, *302*, 1931–1934. [CrossRef]
45. Heard, A.W.; Dauphas, N.; Guilbaud, R.; Rouxel, O.J.; Butler, I.B.; Nie, N.X.; Bekker, A. Triple iron isotope constraints on the role of ocean iron sinks in early atmospheric oxygenation. *Science* **2020**, *370*, 446–449. [CrossRef] [PubMed]
46. Manning, C.V.; McKay, C.P.; Zahnle, K.J. Nitrates on Mars: Evidence from the 15/14N isotopic ratio. In Proceedings of the AGU Fall Meeting, San Francisco, CA, USA, 10–14 December 2007; p. P13D-1556.
47. Sefton-Nash, E.; Catling, D.C.; Wood, S.E.; Grindrod, P.M.; Teanby, N.A. Topographic, spectral and thermal inertia analysis of interior layered deposits in Iani Chaos, Mars. *Icarus* **2012**, *221*, 20–42. [CrossRef]

Disclaimer/Publisher's Note: The statements, opinions and data contained in all publications are solely those of the individual author(s) and contributor(s) and not of MDPI and/or the editor(s). MDPI and/or the editor(s) disclaim responsibility for any injury to people or property resulting from any ideas, methods, instructions or products referred to in the content.